Valence Orbitals Driving the Spin Dynamics in a Rare-Earth Single-Atom Magnet

A. Curcella, D. Sblendorio, S. Rusponi, M. Pivetta, F. Patthey, and H. Brune*
Institute of Physics, Ecole Polytechnique Fédérale de Lausanne, CH-1015 Lausanne, Switzerland

(Received 19 October 2022; revised 17 January 2023; accepted 10 February 2023; published 8 March 2023)

We combine spin-polarized scanning tunneling microscopy with quantum master equation analysis to investigate the spin dynamics of the single atom magnet Dy on graphene/Ir(111). By performing reading and writing experiments, we show that the strongly spin polarized $5d6s$ valence shells, as well as their intra-atomic exchange coupling to the $4f$ shell, determine the pathways for magnetization relaxation and thus the spin dynamics. The good quantum number that determines which states are stable and which mechanisms for reversal exist in a given crystal field is the atomic total angular momentum J_z^{tot} and not the commonly considered J_z^{4f} of the $4f$ shell only.

DOI: 10.1103/PhysRevLett.130.106702

Because of their strongly localized and therefore well-protected $4f$ electrons, rare-earth atoms enabled the realization of single-ion molecular magnets (SIMs) [1–4] and single-atom magnets (SAMs) [5–12]. A fundamental understanding of their spin dynamics is mandatory in the operation of single rare-earth atoms as qubits and memories [13–28].

The occupation of the $4f$ orbitals is well described by Hund's rules, resulting in atomiclike spin and orbital momenta that are strongly coupled. A spin polarization of the valence shells ($5d$ and $6s$) is also frequently expected, however, yielding only a small extra contribution to the total momentum. Consequently, the rare earth atoms' magnetic properties are described exclusively in terms of the total angular momentum of the $4f$ shell, $|J^{4f}\rangle$. Hence, spin dynamics in SAMs and SIMs is explained as transitions between states defined by the $|J^{4f}\rangle$ projection onto the quantization axis $|J_z^{4f}\rangle$ ($4f$ model) [2–6,10,11].

While this approach applies to those cases where the lanthanide atoms are in a $+3$ oxidation state, as in most SIMs, recent theoretical works suggest that this description is not always valid [29,30] and that the valence electrons can play an essential role. For instance, they mediate ferromagnetic exchange coupling in dilanthanide complexes [31,32]. In view of the strong valence-$4f$ intra-atomic exchange coupling, the magnetic state of a rare-earth atom should then be described in terms of the total angular momentum $|J^{\mathrm{tot}}\rangle = |J^{4f}\rangle \otimes |S^{5d}\rangle \otimes |S^{6s}\rangle$, where the total angular momentum of the $5d$ and $6s$ shells is approximated by the spin momentum only, since the orbital momentum of these shells is either zero ($6s$), or strongly quenched by hybridization with the surrounding atoms ($5d$). This scenario implies a paradigm shift and was labeled FV-magnetism [29,30]. If it holds, the spin dynamics is determined by the transition probabilities between the projections of $|J^{\mathrm{tot}}\rangle$ onto the quantization axis, $|J_z^{\mathrm{tot}}\rangle$ ($4f5d6s$ model).

The most important difference between these descriptions is that the associated Hilbert spaces have different channels for quantum tunneling of the magnetization (QTM). In the traditional $4f$ model, and for an atom in a crystal field (CF) with k-fold symmetry, QTM involves states differing by $\Delta J_z^{4f} = kn$, with $n \in \mathbb{Z}$. In the $4f5d6s$ model, QTM takes place via states with $\Delta J_z^{\mathrm{tot}} = kn$.

Here we present direct experimental evidence that the spin dynamics of a rare-earth SAM is determined by FV-magnetism. We use spin-polarized scanning tunneling microscopy (SP-STM) to investigate the magnetization switching rates of individual Dy atoms on graphene on Ir(111) [6] as a function of temperature and tunnel voltage. We find evidence for two low-lying channels for QTM that only exist in the $4f5d6s$ model. Within this model, all switching rates are reproduced by quantum master equations. In contrast, the conventional $4f$ model, which exhibits only one low-energy channel for QTM, fails to describe the experimental results.

We choose Dy/gr/Ir(111), as previous knowledge of this system determines the Hamiltonians predicting the magnetic level schemes for both models, thus enabling the most realistic comparison between the two. X-ray absorption spectroscopy (XAS) and x-ray magnetic circular dichroism (XMCD) reveal a $4f^{10}$ filling with $|J^{4f} = 8\rangle$ and a $|J_z^{4f} = \pm 7\rangle$ ground state with out-of-plane easy magnetization axis. The XMCD magnetization curves exhibit two steps due to level crossings that determine the energy separation of the low-lying doublets [6]. STM reports

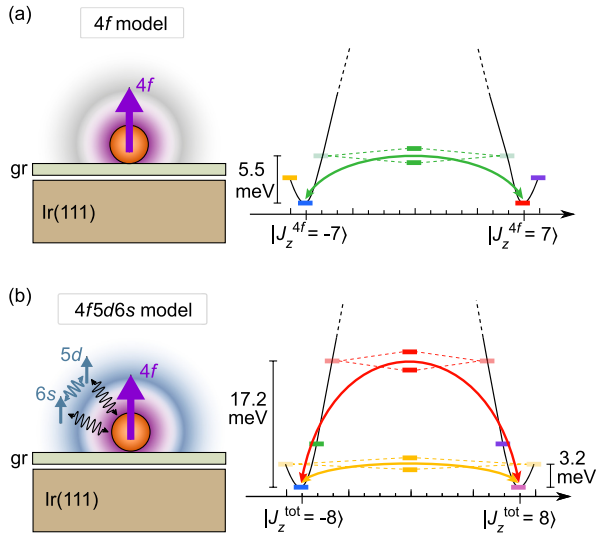

FIG. 1. Sketches (left) and magnetic level schemes (right) of (a) the $4f$ and (b) the $4f5d6s$ model, as determined from published XMCD data. In (a) there is only one QTM path available, via $|J_z^{4f} = \pm 6\rangle$ (green arrow) while in (b) two such paths exist, via $|J_z^{\mathrm{tot}} = \pm 9\rangle$ (yellow) and $|J_z^{\mathrm{tot}} = \pm 6\rangle$ (red). States with the same color are mixed by the sixfold crystal field.

exclusive adsorption in the sixfold graphene hollow site, determining the CF symmetry [6], and SP-STM reveals a large spin polarization of the $5d6s$ shells [33] that is rationalized by the transfer of 0.74 ± 0.03 electrons to the substrate [34]. This valence spin is exchange coupled by almost 100 meV to the spin of the $4f$ shell, and density functional theory (DFT) calculations show that this exchange originates from both, $5d$ and $6s$ shells [33].

The magnetic quantum level schemes accounting for these findings are presented in Fig. 1. The orbital resolved composition, energies, and the splittings of the doublets are given in Table I. The slightly different energies of the excited states in the two models are required to reproduce the steps in the XMCD magnetization curve due to the different Zeeman splittings. In the $4f$ model, the $|J_z^{4f} = \pm 7\rangle$ ground state doublet is protected from QTM and spin reversal takes place via excitation to the split doublet originating from the mixed $|J_z^{4f} = \pm 6\rangle$ states. For the $4f5d6d$ model, an exact evaluation of the spin polarization of the $5d$ and $6s$ shells from DFT is difficult due to the large spatial extent of these orbitals and their hybridization with C $2p$ states; thus, we assume for simplicity a half-integer spin for each valence shell, $S^{5d} = ½$ and $S^{6s} = ½$. Now we get a $|J_z^{\mathrm{tot}} = \pm 8\rangle$ ground state doublet that is again protected from QTM, however, there exist two pathways for magnetization reversal, namely, via the $|J_z^{\mathrm{tot}} = \pm 9\rangle$ and the $|J_z^{\mathrm{tot}} = \pm 6\rangle$ split doublets.

Constant-height tunnel current traces recorded with the STM tip centered on top of isolated Dy adatoms show a two-state telegraph signal due to the magnetization reversal of Dy, see Fig. 2(a). The high conductance (HC) and low conductance (LC) states correspond to parallel and

TABLE I. Out-of-plane projected eigenstates $|J_z^{4f}\rangle$ ($4f$ model) and $|J_z^{\mathrm{tot}}\rangle$ ($4f5d6s$ model), their orbital resolved composition in $\hbar$ units, eigenvalues E, and energy splitting $\hbar\omega$ of the doublets.

	J_z^{4f}	S_z^{5d}	S_z^{6s}	E (meV)	$\hbar\omega$ (μeV)
$\lvert J_z^{4f}\rangle$					
$\lvert \pm 7\rangle$	±7.0	⋯	⋯	0	0
$\lvert \pm 8\rangle$	±8.0	⋯	⋯	3.0	0
$\lvert \pm 6\rangle$	0	⋯	⋯	5.5	13
$\lvert J_z^{\mathrm{tot}}\rangle$					
$\lvert \pm 8\rangle$	±7.1	±0.5	±0.5	0	0
$\lvert \pm 9\rangle$	0	0	0	3.2	0.0036
$\lvert \pm 7\rangle$	±6.3	±0.4	±0.4	5.8	0
$\lvert \pm 6\rangle$	0	0	0	17.2	13

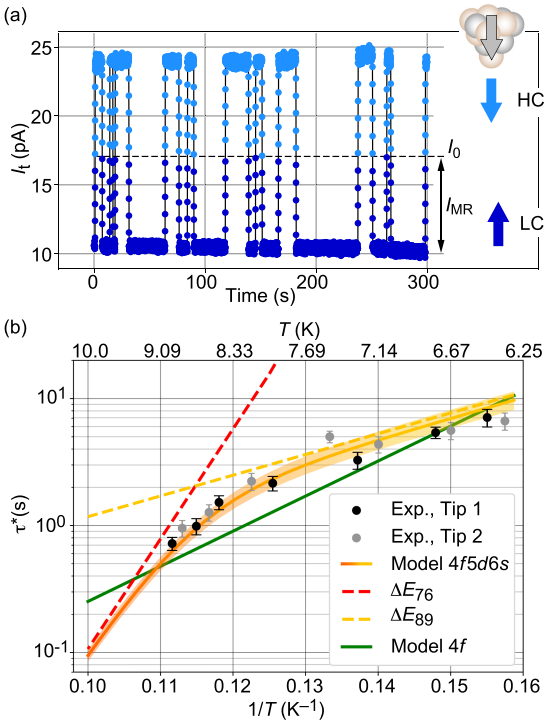

FIG. 2. (a) Telegraph signal of Dy ($T = 6.3$ K, bias voltage $V_b = 1$ mV, set current $I_t = 10$ pA in the LC state). I_0 is the nonpolarized and I_{MR} the magnetoresistive current. Right: alignment of tip spin polarization at E_{F} and Dy momentum in both states. (b) Arrhenius plot of the spin lifetime. Experiment: black and grey dots ($V_b = 1$ mV, set current $I_t = 10$ pA in the LC state). $4f5d6s$ model: red-to-yellow curve, the shaded area shows the accuracy of the fit with $B_{\mathrm{tip}} = -60 \pm 5$ mT. Yellow and red dashed lines show τ^* with QTM exclusively via $|J_z^{\mathrm{tot}} = \pm 9\rangle$ or $|J_z^{\mathrm{tot}} = \pm 6\rangle$, corresponding to activation energies $\Delta E_{89} = E(|J_z^{\mathrm{tot}} = 9\rangle) - E(|J_z^{\mathrm{tot}} = 8\rangle)$ and $\Delta E_{76} = E(|J_z^{\mathrm{tot}} = 6\rangle) - E(|J_z^{\mathrm{tot}} = 7\rangle)$, respectively. $4f$ model: green curve. $\rho_T = -0.8$ for both models.

TABLE II. Hamiltonian terms in the two models.

	$4f$ model	$4f5d6s$ model
J	$J^{4f} = 8$	$J^{\mathrm{tot}} = 9$ $(J^{4f} = 8, S^{5d} = ½, S^{6s} = ½)$
$\hat{H}_{\mathrm{ex}}$	$\cdots$	$(g_J - 1)[\mathcal{J}_{4f-6s}(\hat{J}^{4f} \cdot \hat{S}^{6s}) + \mathcal{J}_{4f-5d}(\hat{J}^{4f} \cdot \hat{S}^{5d})] + \mathcal{J}_{5d-6s}(\hat{S}^{5d} \cdot \hat{S}^{6s})$
$\hat{H}_{\mathrm{CF}}$	$B_2^0\hat{O}_2^0 + B_4^0\hat{O}_4^0 + B_6^0\hat{O}_6^0 + B_6^6\hat{O}_6^6$	$B_2^0\hat{O}_2^0 + B_4^0\hat{O}_4^0 + B_6^0\hat{O}_6^0 + B_6^6\hat{O}_6^6$
$\hat{H}_Z$	$\mu_B g_J J_z^{4f} B_{\mathrm{tip}}$	$\mu_B(g_J J_z^{4f} + g S_z^{sd}) B_{\mathrm{tip}}$
$\hat{H}_{\text{sp-ph}}$	$(\hat{J}_-^{4f})^2 + (\hat{J}_+^{4f})^2 + \{\hat{J}_-^{4f}, \hat{J}_z^{4f}\} + \{\hat{J}_+^{4f}, \hat{J}_z^{4f}\}$	$(\hat{J}_-^{4f})^2 + (\hat{J}_+^{4f})^2 + \{\hat{J}_-^{4f}, \hat{J}_z^{4f}\} + \{\hat{J}_+^{4f}, \hat{J}_z^{4f}\}$
$\hat{H}_{\text{sp-el}}$	$\hat{\sigma} \cdot \hat{J}^{4f}$	$\hat{\sigma} \cdot \hat{S}^{sd}$

antiparallel alignment of the tip and Dy spin polarizations. Note the large spin contrast, expressed by the large fraction of the magnetoresistive to the nonpolarized current, I_{MR} and I_0, respectively. The individual lifetimes of both states, τ_{HC} and τ_{LC}, are determined by fitting histograms of residence times. To describe the spin dynamics, it suffices to consider a single characteristic lifetime, $\tau^* = \tau_{\mathrm{HC}}\tau_{\mathrm{LC}}/(\tau_{\mathrm{HC}} + \tau_{\mathrm{LC}})$ [35]. The occupancies of the individual states are given by $\tau^*/\tau_{\mathrm{HC}}$ and $\tau^*/\tau_{\mathrm{LC}}$.

Figure 2(b) shows the Arrhenius plot of the spin lifetime τ^* under reading conditions, i.e., with a tunnel voltage below any of the excitation energies of the magnetic quantum levels. The spin lifetime decreases with increasing temperature, evidencing thermally assisted magnetization reversal. The data show a transition between a shallow slope at low T and a much steeper one at high T, with the change occurring around 8.3 K. This observation indicates the presence of two reversal paths with different activation energies.

To distinguish quantitatively between both models, the spin dynamics is calculated via a master equation describing the transition probabilities between the eigenstates of the system in the presence of phonon and electron scattering [14,17,21,64,65]. The Hamiltonian can be written as

$$\hat{H} = \hat{H}_{\mathrm{ex}} + \hat{H}_{\mathrm{CF}} + \hat{H}_Z + \hat{H}_{\text{sp-ph}} + \hat{H}_{\text{sp-el}} \qquad (1)$$

with the respective expressions used for these terms in both models listed in Table II and detailed in [35]. The first three terms define the Dy eigenstates displayed in Fig. 1, while $\hat{H}_{\text{sp-ph}}$ and $\hat{H}_{\text{sp-el}}$ describe the Dy spin scattering with phonons and electrons, respectively.

Only a limited number of free parameters is available to reproduce the data, namely, the tip stray field B_{tip} and spin polarization ρ_T, the ratio ζ between inelastic and elastic tunneling, the surface to adatom hopping probability ς_S, and the spin-phonon scattering efficiency ν_{ph} [35]. Two additional fit parameters are the energy E and splitting $\hbar\omega$ of $|J_z^{\mathrm{tot}} = \pm 6\rangle$, while for the remaining eigenstates these quantities are determined from previous XAS and XMCD experiments.

The observed change in slope in Fig. 2(b) is very well reproduced by the $4f5d6s$ model (red-to-yellow curve), while the $4f$ model (green line) completely fails. In both models, the thermally activated spin dynamics is largely dominated by scattering with substrate electrons, while spin-lattice relaxation is almost negligible in the entire temperature range [35]. This is expected since the high stiffness of graphene implies a low phonon density in the low energy range of interest.

In the $4f5d6s$ model and at low temperatures, scattering with substrate electrons induces spin transitions ($\Delta J_z^{\mathrm{tot}} = \pm 1$) driving the Dy spin from the ground doublet $|J_z^{\mathrm{tot}} = \pm 8\rangle$ to the first excited one $|J_z^{\mathrm{tot}} = \pm 9\rangle$, from where the magnetization reverses via QTM. As we increase the temperature, higher energy states become populated, including the high energy split doublet $|J_z^{\mathrm{tot}} = \pm 6\rangle$. Despite being much less populated than $|J_z^{\mathrm{tot}} = \pm 9\rangle$, the larger energy splitting of $|J_z^{\mathrm{tot}} = \pm 6\rangle$ results in a more efficient QTM. The reversal via $|J_z^{\mathrm{tot}} = \pm 6\rangle$ starts to be activated at about 8.3 K, has a nearly equal weight as reversal via $|J_z^{\mathrm{tot}} = \pm 9\rangle$ at roughly 9 K, and largely dominates for $T \geq 10$ K.

The $4f$ model has a single thermal-assisted QTM channel between $|J_z^{4f} = \pm 6\rangle$ resulting in a straight line in the Arrhenius of τ^*. This line is too steep at low T and too shallow at high T compared to the data.

The strength of the $4f5d6s$ model is further confirmed by experiments under writing conditions, where the magnetic quantum states of Dy are manipulated by electrons tunneling from or to the tip. Figures 3(a)–3(c) show the spin lifetime, HC occupancy, and magnetoresistance as a function of bias voltage V_b at $T = 6.7$ K. The experimental data show small variations in τ^* and an almost flat HC occupancy at 50% for $|V_b| \leq 5$ mV, while τ^* is strongly reduced and strong spin-torque effects are observed at higher biases. The experimental behavior is again very well reproduced by the $4f5d6s$ model, while the $4f$ model is clearly unsatisfactory [66]. The ratio of the magnetoresistive to the nonpolarized current in Fig. 3(c) is only matched by the $4f5d6s$ model. Matching it in the $4f$ model results in too short relaxation times compared to the experimental τ^* in Fig. 3(a).

The bias dependence of the HC occupancy illustrates the difference between the two models very well. The measured staircase behavior can only be reproduced by a multipath

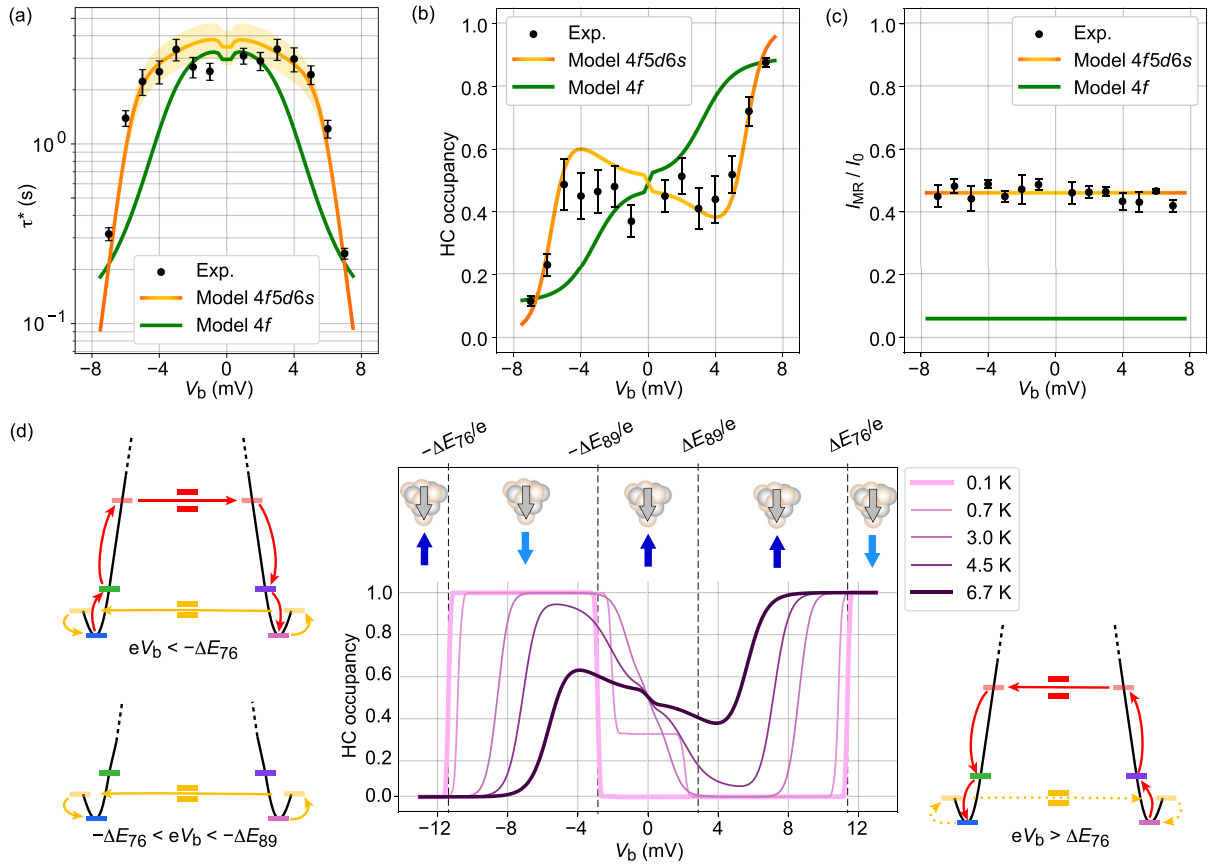

FIG. 3. (a) Spin lifetimes, (b) HC occupancy, and (c) ratio of magnetoresistive to nonpolarized tunneling current vs V_b (black dots, $T = 6.7$ K, set current $I_t = 10$ pA in the LC state). Lines show calculations with the $4f5d6s$ model (red to orange shaded according to QTM via $|J_z^{\rm tot} = \pm 9\rangle$ or $|J_z^{\rm tot} = \pm 6\rangle$) and the $4f$ model (green line) ($B_{\rm tip} = -45$ mT, $\rho_T = -0.8$). The shaded area shows the accuracy of the fit with variations of $B_{\rm tip}$ within ± 5 mT. (d) HC occupancy vs bias predicted by the $4f5d6s$ model for a fully spin-down polarized tip ($B_{\rm tip} = -45$ mT, $\rho_T = -1.0$); top: alignment of tip spin polarization and Dy momentum vs bias. Sketches on the left (right) show the spin reversal pathways for the indicated negative (positive) bias ranges.

reversal model, while a monotonic dependence is predicted by a single-path reversal model. Calculations reported in Fig. 3(d) show that the observed dependence results from steps, appearing at characteristic biases, progressively smoothed with increasing temperature. The origin of these steps is elucidated by looking at the extreme case of 0.1 K and for a fully spin-down polarized tip ($\rho_T = -1.0$) shown as a thick pink line. For $e|V_b| < 3.2$ meV $= \Delta E_{89} = E(|J_z^{\rm tot} = 9\rangle) - E(|J_z^{\rm tot} = 8\rangle)$, only the ground state favored by the tip stray field $|J_z^{\rm tot} = 8\rangle$, with the Dy momentum pointing up, is occupied. Increasing $|V_b|$ opens up inelastic scattering to the next lying eigenstates, progressively activating magnetization reversal pathways. Reaching the first threshold on the negative bias side, where the fully spin-down polarized tip induces $\Delta J_z^{\rm tot} = +1$ transitions, Dy is pumped to $|J_z^{\rm tot} = 9\rangle$, from where the Dy spin tunnels through the barrier to $|J_z^{\rm tot} = -9\rangle$ before relaxing to $|J_z^{\rm tot} = -8\rangle$, see sketch on the lower left in Fig. 3(d). As a result, the Dy spin state switches from $|J_z^{\rm tot} = 8\rangle$ to $|J_z^{\rm tot} = -8\rangle$, corresponding to a HC occupancy of 1 (spin pumping). Backward paths are forbidden since (i) the tunneling current only generates spin-increasing transitions, thus preventing the way back via $|J_z^{\rm tot} = -8\rangle$ to $|J_z^{\rm tot} = -9\rangle$; (ii) at this bias, the electron energy is not sufficient to promote transitions from $|J_z^{\rm tot} = -8\rangle$ to $|J_z^{\rm tot} = -7\rangle$ and farther to the top of the barrier; (iii) spin scattering with phonons and surface conduction electrons has negligible effect at this temperature. Therefore the Dy atom stays frozen in the $|J_z^{\rm tot} = -8\rangle$ state until $eV_b \leq -\Delta E_{76} = -11.4$ meV, where tunneling electrons can promote transitions from there to $|J_z^{\rm tot} = -7\rangle$ and successively to $|J_z^{\rm tot} = -6\rangle$. QTM then induces transitions to $|J_z^{\rm tot} = 6\rangle$, from where the spin can relax to $|J_z^{\rm tot} = 8\rangle$. Note that under these bias conditions, the Dy spin cyclically reverses, see sketch on the upper left in Fig. 3(d). However, the probability of finding it in $|J_z^{\rm tot} = 8\rangle$ is dominant. Writing is obtained by simply stopping the injection of the tunneling current in the desired HC or LC state, as identified via $I_{\rm MR}$.

At positive bias, electrons of the considered tip drive $\Delta J_z^{\rm tot} = -1$ transitions, and consequently they generate transitions from $|J_z^{\rm tot} = 8\rangle$ to $|J_z^{\rm tot} = 7\rangle$, without changing the HC occupancy. Upon reaching the threshold

$eV_b = \Delta E_{76}$, the Dy gets pumped into $|J_z^{\mathrm{tot}} = 6\rangle$. The spin can then tunnel to $|J_z^{\mathrm{tot}} = -6\rangle$, where it relaxes to $|J_z^{\mathrm{tot}} = -8\rangle$. Again, under the effect of a continuous tunneling current, the spin will cyclically switch back to $|J_z^{\mathrm{tot}} = 8\rangle$, via the yellow dotted path shown in the right sketch of Fig. 3(d). However, the probability of finding it in $|J_z^{\mathrm{tot}} = -8\rangle$ is largely dominant.

We have demonstrated that the spin dynamics of Dy atoms on graphene on Ir(111) is governed by FV-magnetism, determining the Hilbert space and the QTM channels available for magnetization reversal. The same is expected to apply to other isolated spins whenever several electronic shells are spin polarized. This goes beyond lanthanides, from 3*d* elements [28,67] to actinides [68], underlining the general implications of our Letter. The role of the polarized valence shells is reminiscent of the one played by delocalized radicals in SIMs where a lanthanide center is exchange coupled with a delocalized radical ligand [69–74], or in dilanthanide radical-bridged complexes [71,75,76]. The radical modifies the spin reversal path and consequently can be used to improve the magnetic stability of the single molecule magnets. However, the strength of this exchange only amounts to a few meV, limiting its effect to temperatures lower than about 30 K [71,76], while the larger FV coupling is expected to determine the spin dynamics up to higher temperatures.

We acknowledge funding from the Swiss National Science Foundation (200020_176932, 200020_204426).

*harald.brune@epfl.ch

[1] N. Ishikawa, M. Sugita, T. Ishikawa, S. Koshihara, and Y. Kaizu, Lanthanide double-decker complexes functioning as magnets at the single-molecular level, J. Am. Chem. Soc. **125**, 8694 (2003).

[2] K. S. Pedersen, A.-M. Ariciu, S. McAdams, H. Weihe, J. Bendix, F. Tuna, and S. Piligkos, Toward molecular 4f single-ion magnet qubits, J. Am. Chem. Soc. **138**, 5801 (2016).

[3] C. A. P. Goodwin, F. Ortu, D. Reta, N. F. Chilton, and D. P. Mills, Molecular magnetic hysteresis at 60 kelvin in dysprosocenium, Nature (London) **548**, 439442 (2017).

[4] F.-S. Guo, B. M. Day, Y.-C. Chen, M.-L. Tong, A. Mansikkamki, and R. A. Layfield, Magnetic hysteresis up to 80 kelvin in a dysprosium metallocene single-molecule magnet, Science **362**, 1400 (2018).

[5] F. Donati, S. Rusponi, S. Stepanow, C. Wäckerlin, A. Singha, L. Persichetti, R. Baltic, K. Diller, F. Patthey, E. Fernandes, J. Dreiser, Ž. Šljivančanin, K. Kummer, C. Nistor, P. Gambardella, and H. Brune, Magnetic remanence in single atoms, Science **352**, 318 (2016).

[6] R. Baltic, M. Pivetta, F. Donati, C. Wäckerlin, A. Singha, J. Dreiser, S. Rusponi, and H. Brune, Superlattice of single atom magnets on graphene, Nano Lett. **16**, 7610 (2016).

[7] F. D. Natterer, K. Yang, W. Paul, P. Willke, T. Choi, T. Greber, A. Heinrich, and C. Lutz, Reading and writing single-atom magnets, Nature (London) **543**, 226 (2017).

[8] F. D. Natterer, F. Donati, F. Patthey, and H. Brune, Thermal and Magnetic-Field Stability of Holmium Single-Atom Magnets, Phys. Rev. Lett. **121**, 027201 (2018).

[9] F. Donati, S. Rusponi, S. Stepanow, L. Persichetti, A. Singha, D. M. Juraschek, C. Wäckerlin, R. Baltic, M. Pivetta, K. Diller, C. Nistor, J. Dreiser, K. Kummer, E. Velez-Fort, N. A. Spaldin, H. Brune, and P. Gambardella, Unconventional Spin Relaxation Involving Localized Vibrational Modes in Ho Single-Atom Magnets, Phys. Rev. Lett. **124**, 077204 (2020).

[10] F. Donati, M. Pivetta, C. Wolf, A. Singha, C. Wäckerlin, R. Baltic, E. Fernandes, J.-G. de Groot, S. Lamia Ahmed, L. Persichetti, C. Nistor, J. Dreiser, A. Barla, P. Gambardella, H. Brune, and S. Rusponi, Correlation between electronic configuration and magnetic stability in dysprosium single atom magnets, Nano Lett. **21**, 8266 (2021).

[11] A. Singha, P. Willke, T. Bilgeri, X. Zhang, H. Brune, F. Donati, A. J. Heinrich, and T. Choi, Engineering atomic-scale magnetic fields by dysprosium single atom magnets, Nat. Commun. **12**, 4179 (2021).

[12] V. Bellini *et al.*, Slow magnetic relaxation of Dy adatoms with in-plane magnetic anisotropy on a two-dimensional electron gas, ACS Nano **16**, 11182 (2022).

[13] S. Bertaina, S. Gambarelli, A. Tkachuk, I. N. Kurkins, B. Malkin, A. Stepanov, and B. Barbara, Rare-earth solid-state qubits, Nat. Nanotechnol. **2**, 39 (2007).

[14] S. Loth, K. von Bergmann, M. Ternes, A. Otte, C. Lutz, and A. Heinrich, Controlling the state of quantum spins with electric currents, Nat. Phys. **6**, 340 (2010).

[15] A. A. Khajetoorians, J. Wiebe, B. Chilian, and R. Wiesendanger, Realizing all-spin–based logic operations atom by atom, Science **332**, 1062 (2011).

[16] R. Vincent, S. Klyatskaya, M. Ruben, W. Wernsdorfer, and F. Balestro, Electronic read-out of a single nuclear spin using a molecular spin transistor, Nature (London) **488**, 357360 (2012).

[17] A. Khajetoorians, B. Baxevanis, C. Hübner, T. Schlenk, S. Krause, T. Wehling, S. Lounis, A. Lichtenstein, D. Pfannkuche, J. Wiebe, and R. Wiesendanger, Current-driven spin dynamics of artificially constructed quantum magnets, Science **339**, 55 (2013).

[18] S. Thiele, F. Balestro, R. Ballou, S. Klyatskaya, M. Ruben, and W. Wernsdorfer, Electrically driven nuclear spin resonance in single-molecule magnets, Science **344**, 1135 (2014).

[19] S. Baumann, W. Paul, T. Choi, C. P. Lutz, A. Ardavan, and A. J. Heinrich, Electron paramagnetic resonance of individual atoms on a surface, Science **350**, 417 (2015).

[20] C. Godfrin, A. Ferhat, R. Ballou, S. Klyatskaya, M. Ruben, W. Wernsdorfer, and F. Balestro, Operating Quantum States in Single Magnetic Molecules: Implementation of Grover's Quantum Algorithm, Phys. Rev. Lett. **119**, 187702 (2017).

[21] W. Paul, K. Yang, S. Baumann, N. Romming, T. Choi, C. P. Lutz, and A. J. Heinrich, Control of the millisecond spin lifetime of an electrically probed atom, Nat. Phys. **13**, 403 (2017).

[22] B. Kiraly, A. N. Rudenko, W. M. J. van Weerdenburg, D. Wegner, M. I. Katsnelson, and A. A. Khajetoorians, An orbitally derived single-atom magnetic memory, Nat. Commun. **9**, 3904 (2018).

[23] K. Yang, W. Paul, S.-H. Phark, P. Willke, Y. Bae, T. Choi, T. Esat, A. Ardavan, A. J. Heinrich, and C. P. Lutz, Coherent spin manipulation of individual atoms on a surface, Science **366**, 509 (2019).

[24] B. Verlhac, N. Bachellier, L. Garnier, M. Ormaza, P. Abufager, R. Robles, M.-L. Bocquet, M. Ternes, N. Lorente, and L. Limot, Atomic-scale spin sensing with a single molecule at the apex of a scanning tunneling microscope, Science **366**, 623 (2019).

[25] L. Malavolti, G. McMurtrie, S. Rolf-Pissarczyk, S. Yan, J. A. J. Burgess, and S. Loth, Minimally invasive spin sensing with scanning tunneling microscopy, Nanoscale **12**, 11619 (2020).

[26] H. Biard, E. Moreno-Pineda, M. Ruben, E. Bonet, W. Wernsdorfer, and F. Balestro, Increasing the Hilbert space dimension using a single coupled molecular spin, Nat. Commun. **12**, 4443 (2021).

[27] L. M. Veldman, L. Farinacci, R. Rejali, R. Broekhoven, J. Gobeil, D. Coffey, M. Ternes, and A. F. Otte, Free coherent evolution of a coupled atomic spin system initialized by electron scattering, Science **372**, 964968 (2021).

[28] X. Zhang, C. Wolf, Y. Wang, H. Aubin, T. Bilgeri, P. Willke, A. J. Heinrich, and T. Choi, Electron spin resonance of single iron phthalocyanine molecules and role of their non-localized spins in magnetic interactions, Nat. Chem. **14**, 5965 (2022).

[29] V. Dubrovin, A. A. Popov, and S. Avdoshenko, Magnetism in Ln molecular systems with $4f$/valence-shell interplay (FV-magnetism), Chem. Commun. **55**, 13963 (2019).

[30] V. Dubrovin, A. A. Popov, and S. M. Avdoshenko, Valence electrons in lanthanide-based single-atom magnets: A paradigm shift in 4f-magnetism modeling and design, Inorg. Chem. Front. **8**, 2373 (2021).

[31] F. Liu, D. S. Krylov, L. Spree, S. M. Avdoshenko, N. A. Samoylova, M. Rosenkranz, A. Kostanyan, T. Greber, A. U. B. Wolter, B. Büchner, and A. A. Popov, Single molecule magnet with an unpaired electron trapped between two lanthanide ions inside a fullerene, Nat. Commun. **8**, 16098 (2017).

[32] C. A. Gould, K. R. McClain, D. Reta, J. G. C. Kragskow, D. A. Marchiori, E. Lachman, E.-S. Choi, J. G. Analytis, R. D. Britt, N. F. Chilton, B. G. Harvey, and J. R. Long, Ultrahard magnetism from mixed-valence dilanthanide complexes with metal-metal bonding, Science **375**, 198 (2022).

[33] M. Pivetta, F. Patthey, I. Di Marco, A. Subramonian, O. Eriksson, S. Rusponi, and H. Brune, Measuring the Intra-Atomic Exchange Energy in Rare-Earth Adatoms, Phys. Rev. X **10**, 031054 (2020).

[34] M. Pivetta, S. Rusponi, and H. Brune, Direct capture and electrostatic repulsion in the self-assembly of rare-earth atom superlattices on graphene, Phys. Rev. B **98**, 115417 (2018).

[35] See Supplemental Material at http://link.aps.org/supplemental/10.1103/PhysRevLett.130.106702 for additional information on experimental and model details, and on the specific role of the individual fit parameters, which includes Refs. [36–63].

[36] R. Gaisch, J. K. Gimzewski, B. Reihl, R. R. Schlittler, M. Tschudy, and W. D. Schneider, Low-temperature ultra-high vacuum scanning tunneling microscope, Ultramicroscopy **42–44**, 1621 (1992).

[37] P. Forrester, T. Bilgeri, F. Patthey, H. Brune, and F. D. Natterer, Antiferromagnetic MnNi tips for spin-polarized scanning probe microscopy, Rev. Sci. Instrum. **89**, 123706 (2018).

[38] P.-G. de Gennes, Sur les propriétés des métaux des terres rares, C.R. Acad. Sci. **247**, 1836 (1958).

[39] P.-G. de Gennes, Interactions indirectes entre couches $4f$ dans les métaux de terres rares, J. Phys. Radium **23**, 510 (1962).

[40] L. L. Hirst, Theory of the coupling between conduction electrons and moments of $3d$ and $4f$ ions in metals, Adv. Phys. **27**, 231 (1978).

[41] S. Blundell, *Magnetism in Condensed Matter* (Oxford University Press, New York, 2001).

[42] R. Skomski, *Simple Models of Magnetism* (Oxford University Press, New York, 1996).

[43] R. Ahuja, S. Auluck, B. Johansson, and M. S. S. Brooks, Electronic structure, magnetism, and Fermi surfaces of Gd and Tb, Phys. Rev. B **50**, 5147 (1994).

[44] R. Baltic, F. Donati, A. Singha, C. Wäckerlin, J. Dreiser, B. Delley, M. Pivetta, S. Rusponi, and H. Brune, Magnetic properties of single rare-earth atoms on graphene/Ir(111), Phys. Rev. B **98**, 024412 (2018).

[45] K. Stevens, Matrix elements and operator equivalents connected with the magnetic properties of rare earth ions, Proc. Phys. Soc. London Sect. A **65**, 209 (1952).

[46] P. Politi, A. Rettori, F. Hartmann-Boutron, and J. Villain, Tunneling in Mesoscopic Magnetic Molecules, Phys. Rev. Lett. **75**, 537 (1995).

[47] C. Cervetti, A. Rettori, M. Pini, A. Cornia, A. Repollés, F. Luis, M. Dressel, S. Rauschenbach, K. Kern, M. Burghard, and L. Bogani, The classical and quantum dynamics of molecular spins on graphene, Nat. Mater. **15**, 164 (2016).

[48] E. Callen and H. B. Callen, Magnetostriction, forced magnetostriction, and anomalous thermal expansion in ferromagnets, Phys. Rev. **139**, A455 (1965).

[49] D. Coffey, J. L. Diez-Ferrer, D. Serrate, M. Ciria, C. de la Fuente, and J. I. Arnaudas, Antiferromagnetic spin coupling between rare earth adatoms and iron islands probed by spin-polarized tunneling, Sci. Rep. **5**, 13709 (2015).

[50] P. Anderson, Localized Magnetic States and Fermi-Surface Anomalies in Tunneling, Phys. Rev. Lett. **17**, 95 (1966).

[51] J. Schrieffer and P. Wolff, Relation between the Anderson and Kondo Hamiltonians, Phys. Rev. **149**, 491 (1966).

[52] J. Appelbaum, Exchange model of zero-bias tunneling anomalies, Phys. Rev. **154**, 633 (1967).

[53] M. Ternes, Spin excitations and correlations in scanning tunneling spectroscopy, New J. Phys. **17**, 063016 (2015).

[54] M. N. Leuenberger and D. Loss, Spin tunneling and phonon-assisted relaxation in Mn_{12}-acetate, Phys. Rev. B **61**, 1286 (2000).

[55] D. Gatteschi, R. Sessoli, and J. Villain, *Molecular Nanomagnets* (Oxford University Press, New York, 2006).

[56] A. Abragam, *The Principles of Nuclear Magnetism* (Clarendon Press, Oxford, 1961).

[57] J. Villain, A. Würger, A. Fort, and A. Rettori, Effet tunnel dans les systèmes magnétiques: de la description microscopique et déterministe à l'équation maîtresse, J. Phys. I (France) **7**, 1583 (1997).

[58] F. Luis, J. Bartolomé, and J. F. Fernández, Resonant magnetic quantum tunneling through thermally activated states, Phys. Rev. B **57**, 505 (1998).

[59] L. Falkovsky, Phonon dispersion in graphene, J. Exp. Theor. Phys. **105**, 397 (2007).

[60] F. D. Natterer, F. Patthey, T. Bilgeri, P. Forrester, N. Weiss, and H. Brune, Upgrade of a low-temperature scanning tunneling microscope for electron-spin resonance, Rev. Sci. Instrum. **90**, 013706 (2019).

[61] A. A. Sapozhnik, C. Luo, H. Ryll, F. Radu, M. Jourdan, H. Zabel, and H. J. Elmers, Experimental determination of exchange constants in antiferromagnetic Mn_2Au, Phys. Rev. B **97**, 184416 (2018).

[62] S. Picozzi and A. Freeman, Polarization reduction in half-metallic Heusler alloys: The effect of point defects and interfaces with semiconductors, J. Phys. Condens. Matter **19**, 315215 (2007).

[63] F. Delgado, J. J. Palacios, and J. Fernández-Rossier, Spin-Transfer Torque on a Single Magnetic Adatom, Phys. Rev. Lett. **104**, 026601 (2010).

[64] A. Fort, A. Rettori, J. Villain, D. Gatteschi, and R. Sessoli, Mixed Quantum-Thermal Relaxation in Mn_{12} Acetate Molecules, Phys. Rev. Lett. **80**, 612 (1998).

[65] F. Delgado and J. Fernández-Rossier, Spin dynamics of current-driven single magnetic adatoms and molecules, Phys. Rev. B **82**, 134414 (2010).

[66] These measurements are characterized by an invariant phonon contribution. Hence, the bias voltage is the only parameter determining the spin reversal path. Identical fit parameters are used for both, temperature and bias dependent experiments, further confirming that spin-phonon scattering is negligible also in the Arrhenius plot.

[67] G. E. Pacchioni, L. Gragnaniello, F. Donati, M. Pivetta, G. Autès, O. V. Yazyev, S. Rusponi, and H. Brune, Multiplet features and magnetic properties of Fe on Cu(111): From single atoms to small clusters, Phys. Rev. B **91**, 235426 (2015).

[68] S. G. McAdams, A.-M. Ariciu, A. K. Kostopoulos, J. P. Walsh, and F. Tuna, Molecular single-ion magnets based on lanthanides and actinides: Design considerations and new advances in the context of quantum technologies, Coord. Chem. Rev. **346**, 216 (2017).

[69] N. Ishikawa, M. Sugita, N. Tanaka, T. Ishikawa, S.-y. Koshihara, and Y. Kaizu, Upward temperature shift of the intrinsic phase lag of the magnetization of bis(phthalocyaninato)terbium by ligand oxidation creating an $S = 1/2$ spin, Inorg. Chem. **43**, 5498 (2004).

[70] M. Urdampilleta, S. Klayatskaya, M. Ruben, and W. Wernsdorfer, Magnetic interaction between a radical spin and a single-molecule magnet in a molecular spin-valve, ACS Nano **9**, 4458 (2015).

[71] S. Demir, I.-R. Jeon, J. R. Long, and T. D. Harris, Radical ligand-containing single-molecule magnets, Coord. Chem. Rev. **289–290**, 149 (2015).

[72] D. Komijani, A. Ghirri, C. Bonizzoni, S. Klyatskaya, E. Moreno-Pineda, M. Ruben, A. Soncini, M. Affronte, and S. Hill, Radical-lanthanide ferromagnetic interaction in a Tb^{III} bis-phthalocyaninato complex, Phys. Rev. Mater. **2**, 024405 (2018).

[73] R. Pederson, A. L. Wysocki, N. Mayhall, and K. Park, Multireference *ab initio* studies of magnetic properties of terbium-based single-molecule magnets, J. Phys. Chem. A **123**, 6996 (2019).

[74] T. Frauhammer, H. Chen, T. Balashov, G. Derenbach, S. Klyatskaya, E. Moreno-Pineda, M. Ruben, and W. Wulfhekel, Indirect Spin-Readout of Rare-Earth-Based Single-Molecule Magnet with Scanning Tunneling Microscopy, Phys. Rev. Lett. **127**, 123201 (2021).

[75] J. D. Rinehart, M. Fang, W. J. Evans, and J. R. Long, A N_2^{3-} radical-bridged terbium complex exhibiting magnetic hysteresis at 14 K, J. Am. Chem. Soc. **133**, 14236 (2011).

[76] S. Demir, M. I. Gonzalez, L. Darago, W. J. Evans, and J. R. Long, Giant coercivity and high magnetic blocking temperatures for N_2^{3-} radical-bridged dilanthanide complexes upon ligand dissociation, Nat. Commun. **8**, 2144 (2017).

Supplemental Material

Valence orbitals driving the spin dynamics in a rare-earth single-atom magnet

A. Curcella, D. Sblendorio, S. Rusponi, M. Pivetta, F. Patthey, and H. Brune

Institute of Physics, Ecole Polytechnique Fédérale de Lausanne, CH-1015 Lausanne, Switzerland

I. EXPERIMENTAL DETAILS

The measurements were performed with a home-built STM operating at liquid He temperature [1]. The sample temperature is measured with a Cernox sensor placed on the STM head. The base pressure during measurements is below $p = 1.0 \times 10^{-10}$ mbar. The Ir(111) single crystal surface is prepared by repeated Ar^+ sputtering (300 K) and annealing (1400 K) cycles. A single layer of graphene is grown by chemical vapor deposition exposing the Ir(111) sample to 100 Langmuir ethylene at 1320 K. Dy atoms are deposited with an *e*-beam evaporator from thoroughly degassed high purity rods (99.9%) at a substrate temperature of roughly 12 K, where surface diffusion is frozen and thus atoms are randomly distributed on the surface [2]. We investigate Dy coverages of 0.002 monolayers, where one monolayer corresponds to one Dy adatom per graphene unit cell. We employ antiferromagnetic $Mn_{88}Ni_{12}$ tips [3], presenting a low residual stray field determined by the majority states. The tip spin-polarization at the Fermi level originates from the minority states and is thus parallel to the tip magnetization. Telegraph signal (TS) traces are acquired with the STM feedback loop open and initialized in the LC state. More than 300 switches between LC and HC states have been acquired for each data point in order to have significant statistics. The Dy spin dynamics is defined via the lifetimes of the LC state (τ_{LC}) and HC state (τ_{HC}), determined by fitting the histograms of residence times. Error bars in the figures correspond to 95 % confidence intervals calculated using the normal approximation interval. Since the stray field of the tip strongly influences our results, each set of measurements has been acquired with the same tip apex, as certified by an unmodified spin contrast.

II. STATE LIFETIMES

The lifetimes of the high conductance τ_{HC} and of the low conductance state τ_{LC} measured in a telegraph noise signal trace can be described by a single effective lifetime $\frac{1}{\tau^*} = \frac{1}{\tau_{\mathrm{HC}}} + \frac{1}{\tau_{\mathrm{LC}}}$ [4]. For brevity, we use indices i and j to refer to the high and low conductance states. The probability of

switching from i to j at time t is given by p_{ij}, while the probability of remaining in the same state is given by p_{ii}. We neglect any transient state, therefore $p_{ij} + p_{ii} = 1$. The time evolution of p_{ii} is given by:

$$p_{ii}(t+dt) = p_{ij}(t)\frac{dt}{\tau_j} + p_{ii}(t)\left(1 - \frac{dt}{\tau_i}\right) = (1-p_{ii}(t))\frac{dt}{\tau_j} + p_{ii}(t)\left(1 - \frac{dt}{\tau_i}\right) = p_{ii}(t) + \frac{dt}{\tau_j} - p_{ii}(t)\frac{dt}{\tau^*} \quad \text{(S1)}$$

where $p_{ij}(t)\frac{dt}{\tau_j}$ represents the fraction of lifetime measurements that contain a switch after dt, while $p_{ii}(t)\left(1 - \frac{dt}{\tau_i}\right)$ is the fraction with no switch. Simplifying further from (S1) gives:

$$\frac{dp_{ii}(t)}{dt} = \frac{1}{\tau_j} - \frac{p_{ii}(t)}{\tau^*} \quad \text{(S2)}$$

Using the initial condition $p_{ii}(0) = 1$ one finds:

$$p_{ii}(t) = \tau^* \left(\frac{1}{\tau_j} + \frac{1}{\tau_i}\exp(-\frac{t}{\tau^*})\right). \quad \text{(S3)}$$

Note that Eq. S2 holds for both states, thus τ^* governs the time evolution of both LC and HC states. The factors $\frac{\tau^*}{\tau_j} = \frac{\tau_i}{\tau_i + \tau_j}$ and $\frac{\tau^*}{\tau_i} = \frac{\tau_j}{\tau_i + \tau_j}$ are the occupancies of the state i and j, respectively.

III. HAMILTONIAN

We discuss the terms of the Hamiltonian in Eq. 1 of the main text, whose expressions are given in Tab. 2 of the main text. Note that the effect of the hyperfine coupling is expected to be negligible in our experimental conditions as discussed in Sec. VI; therefore, it is not included in the Hamiltonian.

A. Exchange energy

The $\hat{H}_{ex}$ term is only present in the $4f5d6s$ model and describes the intra-atomic exchange between the spins of the $4f$ (S^{4f}), the $6s$ (S^{6s}), and the $5d$ (S^{5d}) shells. Following de Gennes notation, we replace the spin S^{4f} with $(g_J - 1)J^{4f}$, g_J being the Landé g factor [5–9]. Because we assume half-integer values for the spins of the outer shells, effective $\mathcal{J}_{4f-5d}$ and $\mathcal{J}_{4f-6s}$ exchange constants have been used in order to match the experimentally observed overall intra-atomic exchange coupling [10]. The exchange interaction between the valence shells, $\mathcal{J}_{6s-5d}$, is strong and has been fixed to 0.5 eV [11].

B. Crystal field

The crystal field Hamiltonian $\hat{H}_{CF}$ contains both, axial and 6-fold transverse terms, in agreement with previous XAS/XMCD works [12, 13]. In both models, the effect of the crystal field is described via an effective spin Hamiltonian acting on the total angular momentum of the $4f$ shell, since this is the only one with a non-vanishing orbital magnetic moment. As a consequence, the Stevens operators $\hat{O}_n^m$ are expressed in terms of $\hat{J}_+^{4f}, \hat{J}_-^{4f}, \hat{J}_z^{4f}$.

Due to the sixfold symmetry of the adsorption site, $\hat{H}_{CF}$ is expressed as the sum of four Stevens operators $\hat{O}_m^n$ [12, 14]:

$$\hat{H}_{CF} = B_2^0\hat{O}_2^0 + B_4^0\hat{O}_4^0 + B_6^0\hat{O}_6^0 + B_6^6\hat{O}_6^6 \tag{S4}$$

where B_2^0, B_4^0, and B_6^0 are the uniaxial parameters. They split the J_z^{tot} states and determine the total zero-field splitting, *i.e.*, the energy difference between the lowest and highest lying J_z^{tot} state, which is equal to the uniaxial magneto-crystalline anisotropy energy. B_6^6 is the transverse CF parameter and mixes J_z^{tot} states that differ by $|J_z^{tot} = \pm 6\rangle$. $\hat{H}_{CF}$ must reproduce the ground state found in XAS measurements, as well as the steps at ± 2.7 T and ± 5.6 T of the XMCD magnetization curves caused by QTM due to level crossings. Consequently, the values of the crystal field parameters for the $4f$ model are taken from Refs. [12, 13]. In the $4f5d6s$ model, these values have been adjusted to take the additional magnetic moment of the $6s$ and $5d$ shells into account, as well as to fit the energy E and splitting $\hbar\omega$ of the $|J_z^{tot} = \pm 6\rangle$ states. The values of both models are listed in Table S1.

TABLE S1. CF Stevens parameters

Model	B_2^0 (μeV)	B_4^0 (neV)	B_6^0 (neV)	B_6^6 (neV)
$4f$	-121	100	1.5	0.3
$4f5d6s$	-518	1047	-0.476	-7.5

C. Zeeman energy

The Zeeman term $\hat{H}_Z$ describes the effect of a magnetic field on the energies of the magnetic quantum levels. All measurements have been performed without an external magnetic field with intent, as the two models show marked differences only when the energy difference between the states in each doublet is small. Therefore, the only magnetic field is the stray field of the tip. It

is assumed homogeneous and perpendicular to sample surface [3]. The tip field gradient can be neglected since the field variation over the size of the atom of interest are well below the width of the shaded area shown in Fig. 2 and Fig. 3 of the main text.

D. Spin-phonon scattering

$\hat{H}_{sp-ph}$ describes spin-lattice relaxation via direct and Orbach scattering mechanisms [15–17]. Transitions with $\Delta J_z^{4f} = \pm 1, \pm 2$ are considered [18], assuming for simplicity an identical value ν_{ph} for all spin-phonon coupling terms. A two-dimensional Debye model is used for the phonon spectrum [17].

E. Spin-electron scattering

$\hat{H}_{sp-el}$ describes the scattering of the electron spin $\hat{\sigma}$ with the Dy. This includes the creation of electron-hole pairs in the tip or in the surface, as well as the inelastic tunneling of an electron from the tip to the surface or vice versa [4, 19–21]. In the $4f5d6s$ model, electrons scatter with the Dy valence shells [22], while in the $4f$ model, they necessarily scatter with the $4f$ shell.

Consistent with previous models [19, 20, 23–26], we use a Kondo-type Hamiltonian where the tip and substrate electrons are treated as reservoirs and Dy as magnetic impurity:

$$\hat{H}_{sp-el} = \sum_{\alpha,\lambda,\lambda',\sigma,\sigma'} T_{\alpha,\lambda,\lambda'} \frac{\tau^{(\alpha)}_{\sigma\sigma'}}{2} \hat{S}_{Dy,\alpha} c^{\dagger}_{\lambda\sigma} c_{\lambda'\sigma'} \tag{S5}$$

where the index α can take on the values x, y, z, and 0. The index $\lambda = (k, \eta)$ refers to the single particle state k in the electrode η. $c^{\dagger}$ (c) creates (annihilates) an electron in the state λ (λ'). We consider the surface and tip as electrodes η, $\eta' \in \{S = \text{surface}, T = \text{tip}\}$, where unprimed indicates the initial and prime the final electrode. The index σ refers to the spin of the tunnel electrons, again distinguishing initial and final electrode without and with prime. $\tau^{(\alpha)}_{\sigma\sigma'}$ are the Pauli matrices and $\hat{S}_{Dy,\alpha}$ the spin operators. In the $4f5d6s$ model, the tunneling electrons scatter directly with the Dy outer shell electrons; thus $\hat{S}_{Dy,\alpha}$ is equal to $\hat{S}_{6s,\alpha}$ or $\hat{S}_{5d,\alpha}$. Consequently, the total angular momentum of the $4f$ shell flips due to the intra-atomic exchange coupling between the shells [10]. On the contrary, in the case of the $4f$ model, $\hat{S}_{Dy,\alpha}$ is replaced by $\hat{J}_{4f,\alpha}$, implying that tunneling electrons interact directly with the internal shell, as it is the only non-vanishing contribution. For $\alpha = 0$, $\tau^{(0)}_{\sigma\sigma'}$ is the identity matrix and T_o the Coulomb potential scattering interaction parameter. For $\alpha = x, y,$ and z, T_α corresponds to the exchange-tunneling interaction parameter between

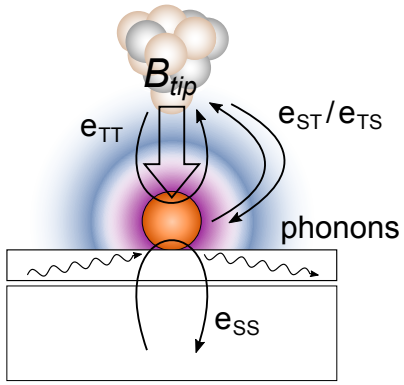

FIG. S1. Sketch of the considered scattering processes.

the tunneling electrons and the Dy adatom. The exchange-tunneling interaction is spin-rotational invariant, thus, $T_x = T_y = T_z \equiv T_k$.

$\hat{H}_{sp-el}$ describes four types of electron scattering: substrate-Dy-substrate scattering (e_{SS}), tip-Dy-tip scattering (e_{TT}), and tip-Dy-substrate/substrate-Dy-tip scattering (e_{TS}/e_{ST}), see Fig. S1. In the case of e_{SS} and e_{TT} scattering, the creation or annihilation of an electron hole pair in the electrodes may induce a spin transition ($\Delta J_z^{tot} = \pm 1$) in the Dy adatom, but does not contribute to the tunneling current like e_{TS} and e_{ST} do.

Since the substrate has no spin polarization at the Fermi level, e_{SS} events induce symmetric $\Delta J_z^{tot} = \pm 1$ transitions and therefore promote equal occupancy between HC and LC states. In the case of tip-Dy-tip scattering, e_{TT} mainly induces spin-increasing ($\Delta J_z^{tot} = +1$) or spin-decreasing ($\Delta J_z^{tot} = -1$) transitions in the Dy adatom, for a tip density of states of spin-up electrons of $\rho_{T\uparrow} > 0.5$ and $\rho_{T\uparrow} < 0.5$, respectively.

The electrons that participate in tip-Dy-substrate/substrate-Dy-tip scattering (e_{TS}/e_{ST}) also induce asymmetric spin transitions due to the spin polarization of the tip. These processes define the inelastic component of the current (I_{in}), as they imply a change in energy of the Dy magnetic quantum levels. The electrons that tunnel through the junction without inducing spin transitions determine the non-polarized (I_0) and magnetoresistive polarized (I_{MR}) components of the elastic tunneling current [19]. Despite being the only component actively contributing to the spin transitions in the Dy adatoms, I_{in} is orders of magnitude smaller than both elastic components I_0 and I_{MR}. Thus, in the TS traces we approximate the current of the HC state and LC states as $I_0 + I_{\mathrm{MR}}$ and $I_0 - I_{\mathrm{MR}}$ (Fig. 2(a) in the main text).

IV. MODELING THE SPIN DYNAMICS

The spin dynamics is described following the formalism presented by Delgado *et al.* [19] for the spin-electron scattering rates, to which we add the description for spin-phonon scattering [16, 17, 27, 28] and QTM rates, as described in Refs. [15, 29, 30]. The time evolution of the population P_M of each spin state $|M\rangle$ is then calculated via the following master equation:

$$\frac{dP_M}{dt} = P_{M'} \sum_M W_{MM'}^{el-ph} - P_M \sum_{M'} W_{MM'}^{el-ph} + W_{M,-M}^{QTM}(P_{-M} - P_M) \tag{S6}$$

in which $|M\rangle$ and $|-M\rangle$ are states of a given doublet, and $W_{MM'}^{el-ph}$ is the sum of all spin-electron and spin-phonon transition rates between initial state $|M\rangle$ and final state $|M'\rangle$:

$$W_{MM'}^{el-ph} = W_{MM'}^{TS} + W_{MM'}^{ST} + W_{MM'}^{SS} + W_{MM'}^{TT} + W_{MM'}^{ph} \tag{S7}$$

This formalism holds only if the linewidth of each level is smaller than the energy difference between any pair of energy levels [31]. In the magnetic field generated by our tip, the energy difference is larger than 1 μeV for any pair. This requires linewidths smaller than 1 μeV or equivalently level lifetimes longer than about 0.6 ns. Since the lifetime of the high energy doublets could not be determined experimentally, we can only provide a qualitative estimation. For Mn atoms on Cu_2N/Cu(100), these lifetimes have been evaluated to about 0.5 ns [20]. In our case we expect much longer lifetimes given the screened nature of the $4f$ states with respect to the $3d$ states of Mn. In addition, our calculations show that the main deexcitation process is the scattering with electrons, see Fig. S2(b). In the experiment we used a current of 10 pA, corresponding to tunneling of one electron roughly every 10 ns; this value sets the lower bound for the lifetime of the excited states. Based on these arguments, we expect to fulfill the condition required to apply the master equation approach.

A. Electron scattering rates

The electron-induced transition rates can be written as:

$$W_{MM'}^{\eta\eta'} = \sum_{\alpha=+,-,z} \left|\langle M'|\hat{S}_{Dy,\alpha}|M\rangle\right|^2 \mathcal{R}_{\alpha,\eta\eta'} \tag{S8}$$

$\mathcal{R}_{\alpha,\eta\eta'}$ is defined as:

$$\mathcal{R}_{\alpha,\eta\eta'} = \frac{2\pi}{\hbar}\zeta^2 \left(\varsigma_\eta \varsigma_{\eta'} \mathcal{Q}_{\alpha,\eta\eta'} \mathcal{F}_{\eta\eta'}(E_{MM'}, \pm eV_b) + \varsigma_\eta^2 Q_{\alpha,\eta\eta} \mathcal{F}_{\eta\eta}(E_{MM'}, \pm 0)\right) \tag{S9}$$

where $\zeta = T_k/T_o$ is the ratio between inelastic and elastic tunneling strengths, and $\mathcal{F}_{\eta\eta'}$ the Fermi-Dirac distribution:

$$\mathcal{F}_{\eta\eta'}(E_{MM'}, \pm eV_b) = \frac{E_{MM'} \pm eV_b}{\exp[(E_{MM'} \pm eV_b)\beta] - 1} \tag{S10}$$

with $\beta = 1/k_{\mathrm{B}}T$. $\mathcal{Q}_{a,\eta\eta'}$ accounts for the polarization of the electrodes:

$$\mathcal{Q}_{+(-),\eta\eta'} = \rho_{\eta\downarrow(\uparrow)}\rho_{\eta'\uparrow(\downarrow)}, \quad \mathcal{Q}_{z,\eta\eta'} = \rho_{\eta\uparrow}\rho_{\eta'\uparrow} + \rho_{\eta\downarrow}\rho_{\eta'\downarrow} \tag{S11}$$

$E_{MM'}$ is the energy difference between the state $|M\rangle$ and $|M'\rangle$. The sign in $E_{MM'} \pm eV_b$ in Eq. S10 is positive for surface to tip tunneling (e_{ST}) and negative for tip to surface tunneling (e_{TS}).

The value of the tip-adatom transmission coefficient ς_T is fixed by the experimental value of the elastic current I_0 and by the choice of the substrate-adatom transmission coefficient ς_S, which we keep as a fit parameter. From Delgado *et al.*:

$$\varsigma_T = \frac{4\hbar I_0}{2e\pi\varsigma_S\left(\mathcal{F}(0, eV_b) - \mathcal{F}(0, -eV_b)\right)\left(\rho_{S\uparrow}\rho_{T\uparrow} + \rho_{S\downarrow}\rho_{T\downarrow}\right)}. \tag{S12}$$

The populations derived in Eq. S6 can then be used to estimate the ratio of the magnetoresistive to the elastic tunneling current [19]:

$$I_{\mathrm{MR}}/I_0 = 2\zeta\frac{\rho_{T\uparrow} - \rho_{T\downarrow}}{\rho_{T\uparrow} + \rho_{T\downarrow}}\frac{\sum_M P_M\langle M|\hat{S}_{Dy,z}|M\rangle}{\sum_M P_M} \tag{S13}$$

where $\dfrac{\rho_{T\uparrow} - \rho_{T\downarrow}}{\rho_{T\uparrow} + \rho_{T\downarrow}}$ is the tip polarization ρ_T.

B. Phonon scattering rates

We assume a 2D phonon bath similar to Ref. [17]. Following the formalism used in [16, 17], the spin-phonon transition rates, associated to phonon absorption and emission, take on the form:

$$W^{ph}_{MM'} = \begin{cases} \dfrac{\nu_{ph}}{\rho_{gr}c^4\hbar^3}\dfrac{E^2_{MM'}}{\exp(\beta E_{MM'}) - 1}w_{4f,MM'} \\ \\ \dfrac{\nu_{ph}}{\rho_{gr}c^4\hbar^3}E^2_{MM'}\left(1 + \dfrac{1}{\exp(\beta E_{MM'}) - 1}\right)w_{4f,MM'} \end{cases} \tag{S14}$$

where $\rho_{gr} = 7.7 \times 10^{-7}$ kg/m^2 is the mass density of graphene and $c = 2.1 \times 10^4$ m/s is the speed of sound in graphene [32]. $w_{4f,MM'}$ are the phonon matrix elements squared (acting only on the $4f$ shell), following the $\hat{H}_{sp-ph}$ Hamiltonian in Table II of main text. ν_{ph} accounts for the coupling between graphene and the Dy adatom and for any other proportionality factors not explicitly mentioned in Eq. S14 (see Refs. [17, 28]). Note that ν_{ph} can be different for transitions with $\Delta J_z^{4f} = \pm 1$ and $\Delta J_z^{4f} = \pm 2$, but for simplicity, we use the same value.

TABLE S2. Fit parameters: tip stray field B_{tip}, electron scattering strength ζ, magnetoelastic Dy-graphene coupling ν_{ph}, substrate-adatom transmission coefficient ς_S, and spin polarization of the tip ρ_T.

Model	Measurement	B_{tip} (mT)	ρ_T	ν_{ph}	ζ	ς_S
$4f5d6s$	Arrhenius	-60 ± 5	-0.8	2×10^{-4}	0.65	6.5×10^{-2}
	Bias	-45 ± 5				
$4f$	Arrhenius	-60 ± 5	-0.8	1×10^{-6}	0.005	6.0×10^{-2}
	Bias	-45 ± 5				

C. QTM rates

The tunneling rate of the magnetization between the states $|M\rangle$ and $|-M\rangle$ of a doublet is described by:

$$W_{M,-M}^{QTM} = \frac{2\tau_M^* \omega_o^2}{1 + (\tau_M^* \omega_1)^2} \tag{S15}$$

where τ_M^* of state $|M\rangle$ is $1/\sum_{M'} W_{MM'}$ (*i.e.*, the sum of all outgoing scattering contributions from state $|M\rangle$) in the absence of QTM, $\omega_o = \Delta E_{M,-M}/\hbar$ in resonance, and $\omega_1 = \Delta E_{M,-M}/\hbar$ out of resonance [15, 29, 30].

V. FIT PARAMETERS

Table S2 lists the fit parameters used for the two models presented in the main text. We expect ζ, ν_{ph}, and ς_S to be independent of measurement conditions within the temperature and bias ranges used in the experiments, whereas the tip stray field B_{tip} and the spin polarization of the tip ρ_T are expected to depend on the tip apex used to record the specific magnetization switching traces. Indeed, for B_{tip} we find slightly different values that reproduce the Arrhenius versus the bias dependent measurements that are recorded with different tip apexes. The two values of B_{tip} are in agreement with the stray fields reported for $Mn_{88}Ni_{12}$ tips [3, 33].

The spin polarization of the tip affects I_{MR} and the saturation occupancy at high biases in Fig. 3(b) of the main paper. We find that a single value of $\rho_T = -0.8$ matches I_{MR} and the HC occupancy for all experimental data sets, see Fig. S2(a). This large value is supported by calculations of Mn-based alloys, predicting full polarization at the Fermi energy [34, 35] and in agreement with the high spin contrast seen in experiment, see Fig. 2(a) of the main text.

This leaves us with only three remaining fit parameters common for all data sets reported in Figs. 2 and 3 of the main text. The magnetoelastic coupling ν_{ph} between the Dy adatom and graphene tends to reduce the state occupancy asymmetry since it competes with the electron spin-torque effect observed at high biases. In order to reproduce our observations shown in Fig. 3(b) of the main paper, we need to limit ν_{ph} to the values shown in Table S2. The small values are consistent with the high lateral stiffness of graphene resulting in a reduced phonon density in the low energy range of interest here. The resulting phonon scattering contribution is shown in Fig. S2(b). For low T it is negligible and for higher T it stays below 10 %. This also holds for the $4f$model that is not shown. Therefore, over all temperatures, the scattering rates are dominated by surface electron scattering and potential temperature dependent changes in the phonon scattering mechanism are not expected to manifest themselves.

From Eqs. S9 and S13, it is seen that ζ defines the electron scattering strength that scales with ζ^2. In addition it determines the magnitude of the magnetoresistive component of the current that scales with ζ. In the $4f$ model, scattering occurs with the internal $4f$ shell, and therefore we need a very low value of ζ to compensate for the high value of $\left|\langle M'|\hat{J}_{4f,\alpha}|M\rangle\right|^2$. This results in the dramatic underestimation of the magnetoresistive current shown in Fig. 3(c) of the main paper. In the $4f5d6s$ model, the electronic scattering occurs with the external shells and we find a ζ value that fits the magnetization switching rates as a function of temperature and bias, and correctly

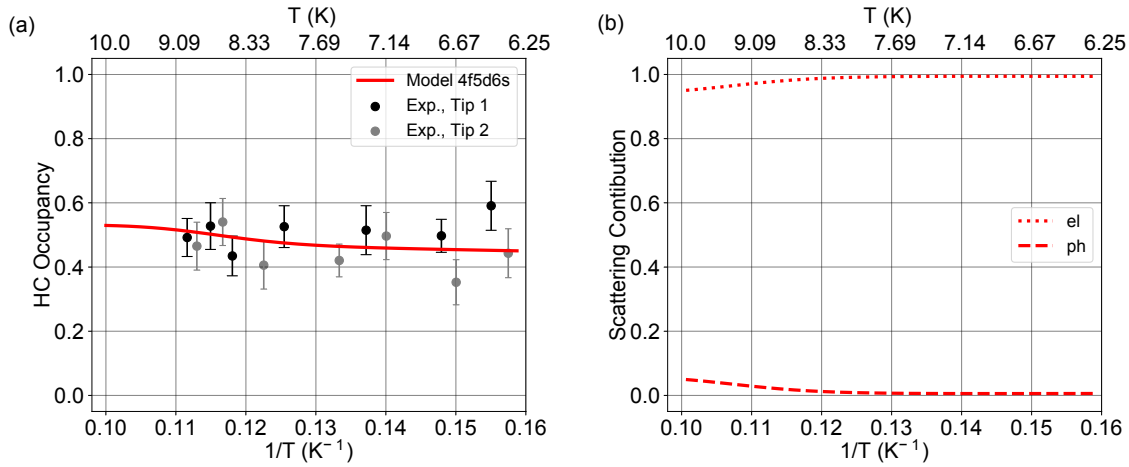

FIG. S2. (a) HC occupancy as a function of $1/T$, black and gray dots show datasets with two different tips (V_b = 1 mV, I_t = 10 pA in the LC state). The full red line shows the $4f5d6s$ model. (b) Electron (el) and phonon (ph) scattering contribution to the spin reversal rate in the Arrhenius plot of $1/\tau^*$ in Fig. 2 of the main text in the $4f5d6s$ model. The scattering contributions are calculated as the ratio of $1/\tau^*_{el/ph}$ to $1/\tau^*_{el+ph}$ with $1/\tau^*_{el+ph} = 1/\tau^*_{ph} + 1/\tau^*_{el}$.

predicts I_{MR}/I_0. This value is similar to the ones reported in Refs. [19, 20, 36]. Note that in $4f$ model smaller values of ζ, and ν_{ph}, are also required to compensate for the increased QTM rate due to the larger splitting of the $|J_z^{4f} = \pm 6\rangle$ doublet with respect to the $|J_z^{tot} = \pm 9\rangle$ one.

The four types of electron scattering described in Sec. IV A are dependent on the tip-adatom and substrate-adatom transmission coefficients ς_T and ς_S. As described in Refs. [19, 36], these transmission coefficients are dependent on tip-adatom and substrate-adatom hopping integrals and the Coulomb potential scattering interaction T_o. As evident from Eq. S12, the elastic current is proportional to $\varsigma_T\varsigma_S$, while substrate-Dy-substrate scattering and tip-Dy-tip scattering are proportional to ς_S^2 and ς_T^2, respectively. Because both coefficients are unknown, and in order to reduce the number of fit parameters, we keep only ς_S as a fit parameter, while we calculate ς_T with Eq. S12. Note that the tip-adatom distance dependence of ς_T, as expected for a hopping integral, is built into Eq. S12 for a given set of tunneling parameters I_t and V_b. Unlike ζ, ς_S has a non-trivial effect on the determination of τ^* when changing tunneling parameters I_t or V_b. While this is not relevant for the measurements taken as a function of temperature, it is relevant for the measurements taken as a function of tunnel bias V_b. For the measurements shown in Fig. 3(a), an increase in ς_S has the effect of decreasing the lifetimes at lower biases (by increasing the strength of substrate scattering), and increasing the lifetimes at higher biases (by decreasing the strength of tip scattering through Eq. S12). This "squeezes" the total range of τ^* spanned in the bias range probed. A decrease in ς_S has the opposite effect – the total range of τ^* spanned is "stretched". A modest change of ς_S by ± 10 % produces a trend inconsistent with experimental observations. This behavior is true for both the $4f$ model and the $4f5d6s$ model. However, it is important to note that this does not influence the fundamental shape of the model prediction in either case, which is derived solely from the available QTM pathways.

VI. EFFECT OF NUCLEAR SPIN

The hyperfine coupling can contribute to open quantum tunneling channels. However, the hyperfine interaction is weak, therefore the induced splittings are very small (a few tens of μeV). Consequently, at the temperature used in our experiments, we expect the hyperfine coupling to have no or only marginal effect on the spin dynamics.

This is in agreement with our observation of no significant difference between individual Dy species that have two nuclear spins with almost equal natural abundancy, namely 44 % have $I = 5/2$ and 56 % $I = 0$.

Similarly, within the error bar given by the uncertainty of the tip stray field, the spin dynamics calculations show no difference between the two nuclear spin species, see Fig. S3.

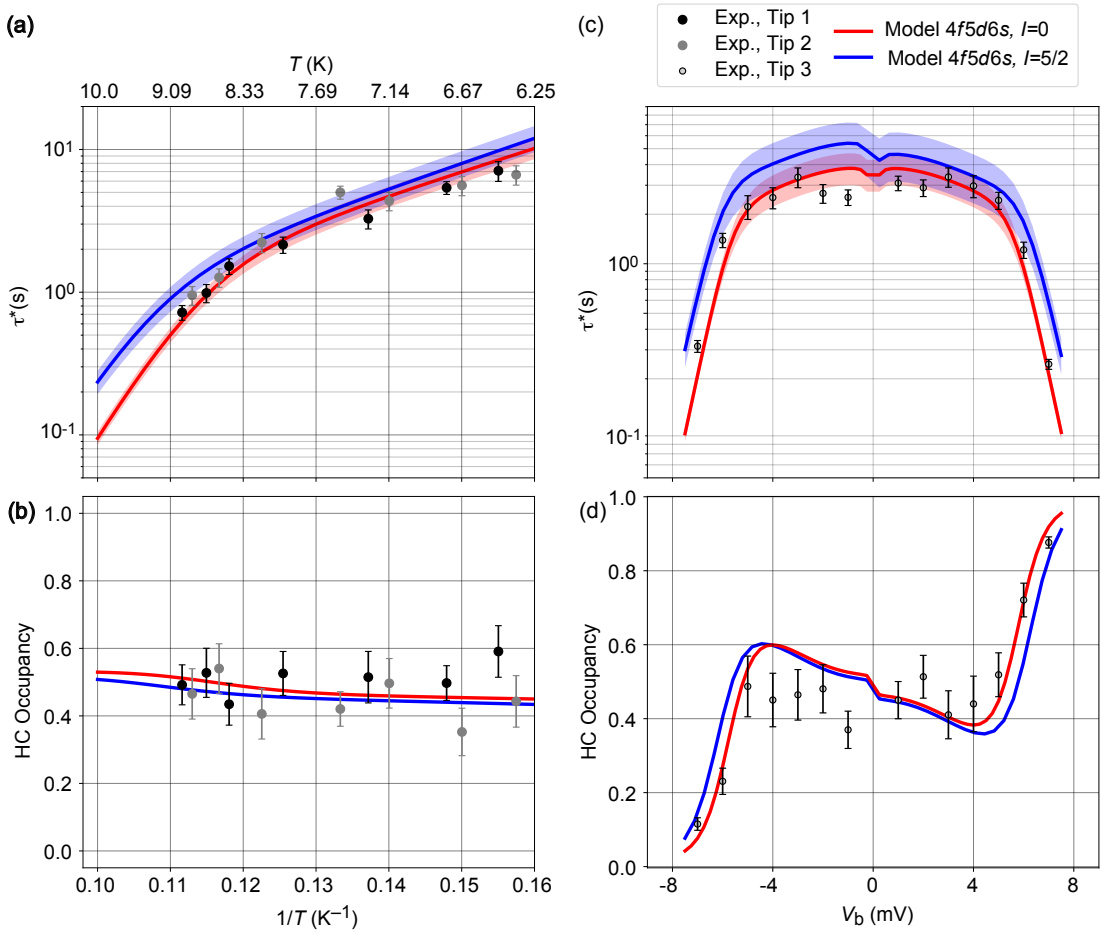

FIG. S3. **Comparing the $4f5d6s$ model with and without nuclear spin I.** (a) Arrhenius plot of the spin lifetime (black and grey dots, $V_b = 1$ mV, set current $I_t = 10$ pA, in the LC state) and (b) corresponding occupancy with fits using the $4f5d6s$ model with nuclear spin (blue) and without (red) (tip polarization $\rho_T = -0.8$, $B_{tip} = -60$ mT in both cases). (c) Spin lifetimes and (d) occupancy as a function of bias V_b (grey dots with black edges and bars, $T = 6.7$ K, set current $I_t = 10$ pA in the LC state). $4f5d6s$ model with nuclear spin (blue) and without (red), using $B_{tip} = -45$ mT, $\rho_T = -0.8$. The shaded areas show the accuracy of the fits with variations of tip magnetic field within ± 5 mT.

[1] R. Gaisch, J. K. Gimzewski, B. Reihl, R. R. Schlittler, M. Tschudy, and W. D. Schneider, Low-temperature ultra-high vacuum scanning tunneling microscope, Ultramicroscopy **42-44**, 1621 (1992).

[2] M. Pivetta, S. Rusponi, and H. Brune, Direct capture and electrostatic repulsion in the self-assembly of rare-earth atom superlattices on graphene, Phys. Rev. B **98**, 115417 (2018).

[3] P. Forrester, T. Bilgeri, F. Patthey, H. Brune, and F. D. Natterer, Antiferromagnetic MnNi tips for spin-polarized scanning probe microscopy, Rev. Sci. Instrum. **89**, 123706 (2018).

[4] A. Khajetoorians, B. Baxevanis, C. Hübner, T. Schlenk, S. Krause, T. Wehling, S. Lounis, A. Lichtenstein, D. Pfannkuche, J. Wiebe, and R. Wiesendanger, Current-driven spin dynamics of artificially constructed quantum magnets, Science **339**, 55 (2013).

[5] P.-G. de Gennes, Sur les propriétés des métaux des terres rares, C. R. Acad. Sc. **247**, 1836 (1958).

[6] P.-G. de Gennes, Interactions indirectes entre couches $4f$ dans les métaux de terres rares, J. Phys. Radium **23**, 510 (1962).

[7] L. L. Hirst, Theory of the coupling between conduction electrons and moments of $3d$ and $4f$ ions in metals, Adv. Phys. **27**, 231 (1978).

[8] S. Blundell, *Magnetism in Condensed Matter* (Oxford University Press, New York, 2001).

[9] R. Skomski, *Simple Models of Magnetism* (Oxford University Press, New York, 1996).

[10] M. Pivetta, F. Patthey, I. Di Marco, A. Subramonian, O. Eriksson, S. Rusponi, and H. Brune, Measuring the intra-atomic exchange energy in rare-earth adatoms, Phys. Rev. X **10**, 031054 (2020).

[11] R. Ahuja, S. Auluck, B. Johansson, and M. S. S. Brooks, Electronic structure, magnetism, and Fermi surfaces of Gd and Tb, Phys. Rev. B **50**, 5147 (1994).

[12] R. Baltic, M. Pivetta, F. Donati, C. Wäckerlin, A. Singha, J. Dreiser, S. Rusponi, and H. Brune, Superlattice of single atom magnets on graphene, Nano Lett. **16**, 7610 (2016).

[13] R. Baltic, F. Donati, A. Singha, C. Wäckerlin, J. Dreiser, B. Delley, M. Pivetta, S. Rusponi, and H. Brune, Magnetic properties of single rare-earth atoms on graphene/Ir(111), Phys. Rev. B **98**, 024412 (2018).

[14] K. Stevens, Matrix elements and operator equivalents connected with the magnetic properties of rare earth ions, Proc. Phys. Soc. A **65**, 209 (1952).

[15] A. Fort, A. Rettori, J. Villain, D. Gatteschi, and R. Sessoli, Mixed quantum-thermal relaxation in Mn_{12} acetate molecules, Phys. Rev. Lett. **80**, 612 (1998).

[16] P. Politi, A. Rettori, F. Hartmann-Boutron, and J. Villain, Tunneling in mesoscopic magnetic molecules, Phys. Rev. Lett. **75**, 537 (1995).

[17] C. Cervetti, A. Rettori, M. Pini, A. Cornia, A. Repollés, F. Luis, M. Dressel, S. Rauschenbach, K. Kern, M. Burghard, and L. Bogani, The classical and quantum dynamics of molecular spins on graphene, Nat. Mater. **15**, 164 (2016).

[18] E. Callen and H. B. Callen, Magnetostriction, forced magnetostriction, and anomalous thermal expan-

sion in ferromagnets, Phys. Rev. **139**, A455 (1965).

[19] F. Delgado and J. Fernández-Rossier, Spin dynamics of current-driven single magnetic adatoms and molecules, Phys. Rev. B **82**, 134414 (2010).

[20] S. Loth, K. von Bergmann, M. Ternes, A. Otte, C. Lutz, and A. Heinrich, Controlling the state of quantum spins with electric currents, Nat. Phys. **6**, 340 (2010).

[21] W. Paul, K. Yang, S. Baumann, N. Romming, T. Choi, C. P. Lutz, and A. J. Heinrich, Control of the millisecond spin lifetime of an electrically probed atom, Nat. Phys. **13**, 403 (2017).

[22] D. Coffey, J. L. Diez-Ferrer, D. Serrate, M. Ciria, C. de la Fuente, and J. I. Arnaudas, Antiferromagnetic spin coupling between rare earth adatoms and iron islands probed by spin-polarized tunneling, Sci. Rep. **5**, 13709 (2015).

[23] P. Anderson, Localized magnetic states and Fermi-surface anomalies in tunneling, Phys. Rev. Lett. **17**, 95 (1966).

[24] J. Schrieffer and P. Wolff, Relation between the Anderson and Kondo Hamiltonians, Phys. Rev. **149**, 491 (1966).

[25] J. Appelbaum, Exchange model of zero-bias tunneling anomalies, Phys. Rev. **154**, 633 (1967).

[26] M. Ternes, Spin excitations and correlations in scanning tunneling spectroscopy, New J. Phys. **17**, 063016 (2015).

[27] M. Leuenberger and D. Loss, Spin tunneling and phonon-assisted relaxation in Mn_{12}-acetate, Phys. Rev. B **61**, 1286 (2000).

[28] R. Gatteschi, D.and Sessoli and J. Villain, *Molecular Nanomagnets* (Oxford University Press, 2006).

[29] A. Abragam, *The Principles of Nuclear Magnetism* (Clarendon Press, Oxford, 1961).

[30] J. Villain, A. Würger, A. Fort, and A. Rettori, Effet tunnel dans les systèmes magnétiques : de la description microscopique et déterministe à l'équation maîtresse, J. Phys. I France **7**, 1583 (1997).

[31] F. Luis, J. Bartolomé, and J. F. Fernández, Resonant magnetic quantum tunneling through thermally activated states, Phys. Rev. B **57**, 505 (1998).

[32] L. Falkovsky, Phonon dispersion in graphene, J. Exp. Theor. Phys. **105**, 397 (2007).

[33] F. D. Natterer, F. Patthey, T. Bilgeri, P. Forrester, N. Weiss, and H. Brune, Upgrade of a low-temperature scanning tunneling microscope for electron-spin resonance, Rev. Sci. Instrum. **90**, 013706 (2019).

[34] A. Sapozhnik, C. Luo, H. Ryll, F. Radu, M. Jourdan, H. Zabel, and H. Elmers, Experimental determination of exchange constants in antiferromagnetic Mn_2Au, Phys. Rev. B **97**, 184416 (2018).

[35] S. Picozzi and A. Freeman, Polarization reduction in half-metallic Heusler alloys: the effect of point defects and interfaces with semiconductors, J. Phys.: Condens. Matter **19**, 315215 (2007).

[36] F. Delgado, J. J. Palacios, and J. Fernández-Rossier, Spin-transfer torque on a single magnetic adatom, Phys. Rev. Lett. **104**, 026601 (2010).